The Astrophysical Journal, 845:100 (9pp), 2017 August 20 https://doi.org/10.3847/1538-4357/aa7de0

Chromospheric Inversions of a Micro-flaring Region

A. Reid[1,2], V. Henriques[1,3], M. Mathioudakis[1], J. G. Doyle[2], and T. Ray[4]
[1] Astrophysics Research Centre, School of Mathematics and Physics, Queen's University Belfast, BT7 1NN, Northern Ireland, UK; aaron.reid@qub.ac.uk
[2] Armagh Observatory and Planetarium, College Hill, Armagh, BT61 9DG, UK
[3] Institute of Theoretical Astrophysics, University of Oslo, P.O. Box 1029 Blindern, NO-0315 Oslo, Norway
[4] Dublin Institute for Advanced Studies, 31 Fitzwilliam Place, Dublin 2, Ireland
Received 2017 April 25; revised 2017 June 9; accepted 2017 June 30; published 2017 August 16

Abstract

We use spectropolarimetric observations of the Ca II 8542 Å line, taken from the Swedish 1 m Solar Telescope, in an attempt to recover dynamic activity in a micro-flaring region near a sunspot via inversions. These inversions show localized mean temperature enhancements of ∼1000 K in the chromosphere and upper photosphere, along with co-spatial bi-directional Doppler shifting of 5–10 km s^{-1}. This heating also extends along a nearby chromospheric fibril, which is co-spatial to 10–15 km s^{-1} downflows. Strong magnetic flux cancellation is also apparent in one of the footpoints, and is concentrated in the chromosphere. This event more closely resembles that of an Ellerman Bomb, though placed slightly higher in the atmosphere than what is typically observed.

Key words: Sun: activity – Sun: chromosphere – Sun: flares – Sun: photosphere

Supporting material: animations

1. Introduction

Micro-flares are considered as events with energies of $\sim10^{26}$–10^{28} erg, and are generally formed as a result of magnetic reconnection in the chromosphere or above (Cauzzi et al. 2001; Chifor et al. 2008; Archontis & Hansteen 2014; Hong et al. 2016). Various magnetic configurations can lead to this reconnection, with the most prominent cause in the literature being due to emerging magnetic flux interacting with a pre-existing magnetic field structure (Kano et al. 2010; Shimizu 2011; Jiang et al. 2012; Leiko & Kondrashova 2015).

Most micro-flares recorded in the literature appear to be rooted in the chromosphere while showing strong responses in higher energy coronal lines (Chifor et al. 2008; Brosius & Holman 2010; Chen & Ding 2010; Hannah et al. 2011; Gontikakis et al. 2013), which are most similar in appearance to flares, only on a smaller scale. Due to their appearance in coronal lines, this has indicated upper temperatures for these events of the order of 1×10^7 K (Chifor et al. 2008).

Bi-directional flows at micro-flaring locations are also commonly reported, with typical values ranging from ±40–80 km s^{-1} (Berkebile-Stoiser et al. 2009; Chen & Ding 2010; Archontis & Hansteen 2014; Leiko & Kondrashova 2015; Hong et al. 2016). Numerical simulations of chromospheric micro-flares due to magnetic reconnection appear to also show bi-directional flows either side of the X-point, with the upflow appearing with a higher velocity than the downflow (Jiang et al. 2010). Surges from these locations have also been reported (Zuccarello et al. 2011; Jiang et al. 2012).

Ellerman Bombs (EBs, Ellerman 1917) are localized photospheric reconnection (Georgoulis et al. 2002; Watanabe et al. 2008; Vissers et al. 2013), with flux cancellation rates circa 10^{14}–10^{15} Mx s^{-1} (Reid et al. 2016). Their main observational signature is the brightening in the wings of the Hα and Ca II 8542 Å line profiles without disturbing the line cores (Rutten et al. 2013; Vissers et al. 2013; Hong et al. 2014). As such, EBs are thought to have no effect on the chromosphere or upper solar atmosphere (Rutten et al. 2013; Vissers et al. 2013) and are considered as solely upper photospheric/lower chromospheric phenomena. Chromospheric surges in Hα have been reported (Yang et al. 2013; Reid et al. 2015), though these are rarely observed and do not enhance the Hα line core.

Semi-empirical modeling attempts of EBs show local temperature enhancements of ∼600–3000 K at the temperature minimum region (Fang et al. 2006; Berlicki et al. 2010; Berlicki & Heinzel 2014; Li et al. 2015; Grubecka et al. 2016), while recent radiative hydrodynamical modeling appears to show similar results (Reid et al. 2017). Bi-directional flows have also been reported in EBs, with the upflows showing a higher velocity than the downflows at EB locations, with values much lower than that of micro-flares (±5 km s^{-1}; Isobe et al. 2007; Matsumoto et al. 2008; Archontis & Hood 2009; Reid et al. 2017).

A recent study by Hansteen et al. (2017) simulates reconnection events in the solar atmosphere and shows the difference in atmospheric conditions for EBs, micro-flares, and UV bursts. They found EBs at localized reconnection sites in the photosphere, with temperatures below 10,000 K and bi-directional flows of up to ∼20 km s^{-1}. The micro-flares appeared as reconnection along a polarity inversion line, with temperature enhancements stretching from its base in the chromosphere to the corona, with values of ∼1 MK and bi-directional flows of up to ±75 km s^{-1}. The simulated UV bursts were then a middle ground between these two reconnection topologies, with the chromospheric/transition region heating up to 10^5 K and flows up to ±50 km s^{-1}.

The similarities between EBs and micro-flares has been noted previously (Berlicki & Heinzel 2014), with Jess et al. (2010), showing evidence of a forced reconnection in the photosphere and labeling it as both a micro-flare and EB. This event also featured bi-directional flows more in-line with EB values, along with Hα wing enhancements.

In this paper, we use the NICOLE inversion code (Socas-Navarro et al. 2015) in an attempt to recover the atmospheric parameters surrounding a chromospheric brightening. Section 2 discusses the observational setup and data reduction. Section 3 discusses the optimization of the inversions, while Sections 4 and 5 show the results and analysis of the final inverted data.

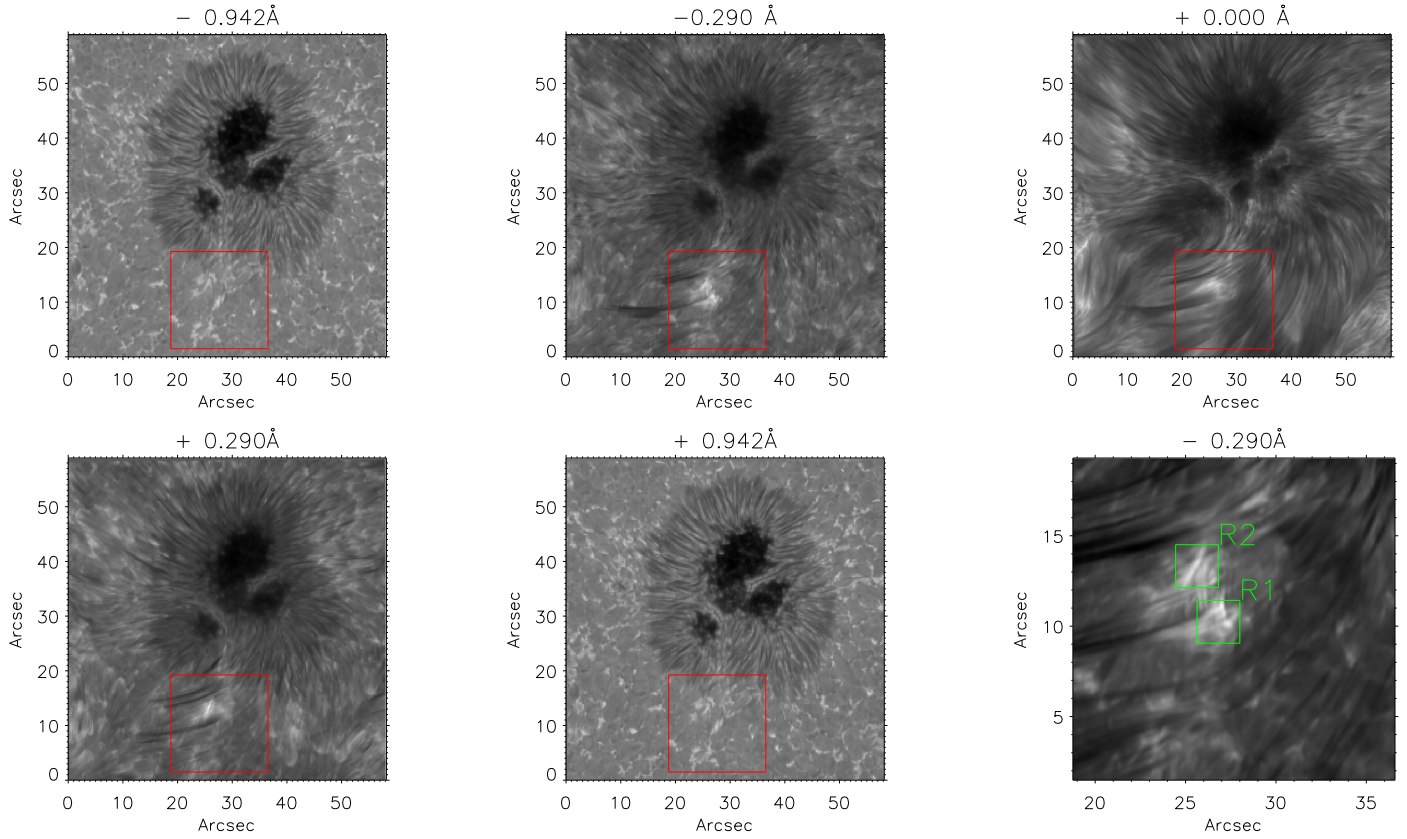

Figure 1. Images at various wavelengths across the Ca II 8542 Å line profile, showing the micro-flare event and connected fibril. The red box highlights the area shown in the bottom right panel. The green boxes show the bright regions (labeled as R1 and R2).

(An animation of this figure is available.)

2. Observations

The observations were carried out with the CRisp Imaging SpectroPolarimeter (CRISP) at the Swedish 1 m Solar Telescope (Scharmer et al. 2003, 2008) on La Palma. The target was the active region NOAA 12121, which is near disk center (coordinates: $X = 40''$, $Y = 40''$, $\mu = 0.99$). The observations took place on 2014 July 28 between 10:43 and 11:24 UT. The observations comprised of imaging spectropolarimetry along the Ca II 8542 Å line. The scan consisted of 15 line positions, taken at ±0.942 Å, ±0.580 Å, ±0.398 Å. ±0.290 Å, ±0.217 Å, ±0.145 Å, ±0.073 Å, and line center. The data had a post-reduction mean cadence of 30 s and a pixel resolution of $0\farcs059$/pix. Sample images from the reduced data set can be seen in Figure 1. The field-of-view (FOV) of the data set is $59 \times 58''$.

The data was processed with the Multi-Object Multi-Frame Blind Deconvolution (MOMFBD) algorithm (Löfdahl 2002; van Noort et al. 2005). This includes tessellation of the images into 64×64 pixels^2 sub-images for individual restoration to preserve the assumption of invariance of the image formation models. An extended MOMFBD scheme that includes the reconstruction of auxiliary wide-band images, co-temporal with the narrow-band wavelengths, and polarizer states were used together with de-stretching (Shine et al. 1994) to reduce the impact of residual seeing on the profiles and on cross-talk (Henriques 2012). A prefilter FOV and wavelength dependent corrections were applied to the restored images. Further information on the general MOMFBD pipeline is available in de la Cruz Rodríguez et al. (2015).

A brightening can be seen in the line core just below the sunspot in Figure 1, as well as in the line wings, where it appears most prominently. This brightening has small footpoints in the far wings of the Ca II 8542 Å observations, where the photosphere is sampled. This brightening therefore stretches from the photosphere up to the mid-chromosphere, with its main enhancements occurring below the canopy. Some small sub-structure can also be seen in the brightening, showing that the initial ball of emission appears to split into two brightened regions. Both of these regions appear to visibly connect to a dark overlying chromospheric fibril (best seen in the −0.290 Å images of Figure 1).

Co-aligned *Solar Dynamics Observatory* (*SDO*) Atmospheric Imaging Assembly (AIA, Lemen et al. 2012), and Helioseismic and Magnetic Imager (HMI, Schou et al. 2012) data were also created in an attempt to locate the same brightening in the transition region or coronal lines. A minor enhancement is apparent in the 1600 and 1700 Å channels of *SDO*, but no upper atmospheric response to this event was visible. An overlying filament is apparent in the upper atmospheric lines of AIA (especially He II 304 Å) and may block any emission of the brightened/ event below.

3. NICOLE Inversions

NICOLE is a parallelized code that solves multi-level, non-local thermodynamic equilibrium (NLTE) problems following

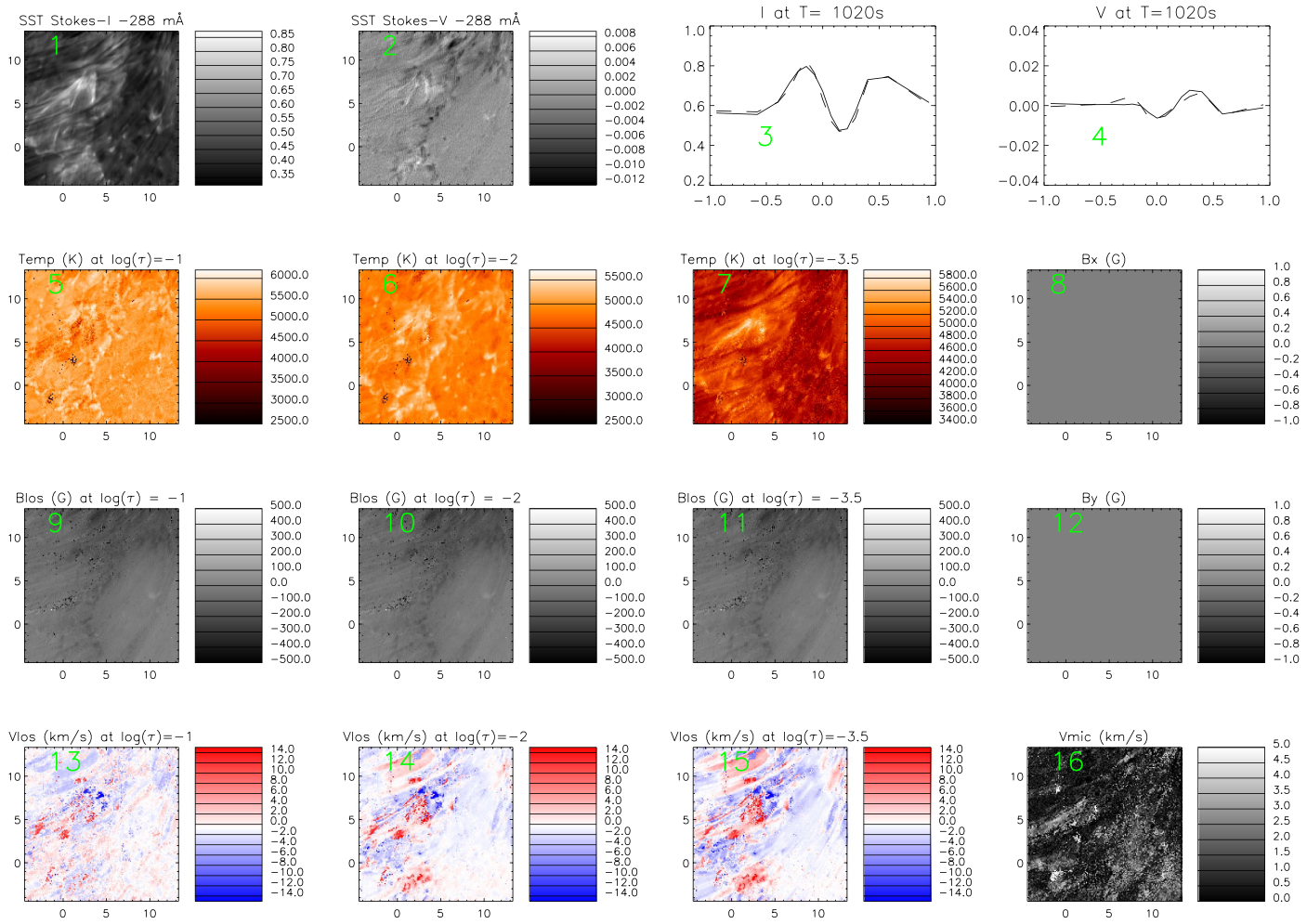

Figure 2. Panel 1: the inverted Stokes-*I* observations at −288 mÅ from line core. Panel 2: co-spatial Stokes-*V* observations in −288 mÅ from line core. Panel 3: the Stokes-*I* line profiles of the observations (solid line) and the synthetic, fitted profiles from the inversions (dashed line). The line profiles are taken from a pixel within the brightening. Panel 4: the Stokes-*V* line profiles, co-spatial to Stokes-*I*. Panels 5–7: the NICOLE output model showing the temperatures at various optical depths. Panel 8: a transverse component of magnetic field. Panels 9–11: the line-of-sight magnetic flux density at various optical depths. Panel 12: the secondary transverse component of magnetic field. Panels 13–15: line-of-sight velocity at various optical depths (positive = downflow). Panel 16: microturbulent velocity (km s^{-1}).

the preconditioning approach described in Socas-Navarro & Trujillo Bueno (1997), while also taking into account polarization of the light via Zeeman splitting. NICOLE uses response functions combined with standard fitting techniques to obtain an atmospheric model that best describes the observed Stokes profiles (Socas-Navarro et al. 1998). The inversions require an initial model to be perturbed, which contains parameters such as a temperature profile, line-of-sight velocity, magnetic field vector, electron density, and microturbulence.

The electron and gas pressures are attained by inserting the temperature stratification into an equation of state with hydrostatic equilibrium imposed and an upper boundary in electron pressure. NICOLE also assumes isotropic scattering and complete frequency redistribution (CRD). While the resonant lines of Ca II H & K require partial redistribution to be fully modeled, the Ca II 8542 Å line can be accurately synthesized in CRD. NICOLE operates in 1.5D, whereby each pixel is individually inverted with its own independent atmosphere. While NICOLE uses a plane parallel atmosphere, radiation comes from and scatters to all directions (I− and I+), with each direction seeing a different effective atmosphere. The correct radiation field is important when computing the NLTE populations of the different levels. NICOLE supports up to five angles along a Gaussian quadrature (see e.g., Section 5.1.2 of Rutten 2003 for further details of such numerical approximation in this context). We selected three angles, which is a common compromise between accuracy and speed.

The Ca II 8542 Å line transition occurs between a 4P–3D shell, with an effective landé factor of $g_{\rm eff} = 1.1$. The nuclear angular momentum of the Ca II atom is non-zero ($F \neq 0$), and as such, small hyperfine structure will also be apparent in the resultant Zeeman-induced profiles. However, this hyperfine splitting is below 1 pm, and therefore will not largely affect our observations (Leenaarts et al. 2014). The NICOLE atomic and line transition data for Ca II 8542 Å were added into their associated look-up libraries within NICOLE, along with five isotopes, to include fine structure.

Due to the contribution function of Ca II 8542 Å encompassing a broad range of heights along the photosphere and chromosphere (Cauzzi et al. 2008; Reid et al. 2017), some stratification with height would also be necessary in order to fully utilize the observations.

The input observations were optimized in order to accumulate a sufficient signal in Stokes-*Q*, -*U*, and -*V*. The

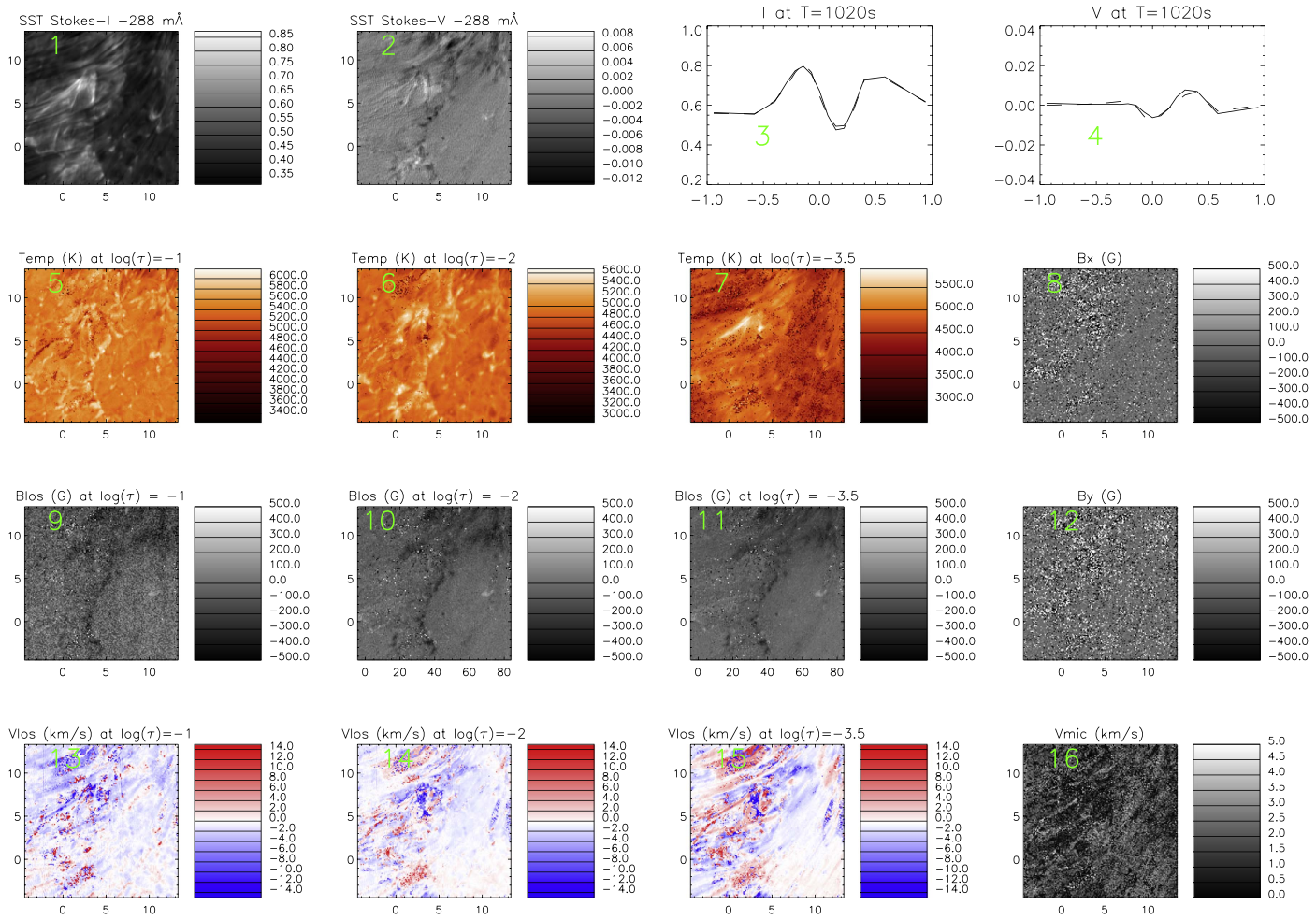

Figure 3. Inversion outputs for the 7 node inversion. The description of the panels is identical to those in Figure 2. The animation shows the temporal evolution from the inversion outputs.

(An animation of this figure is available.)

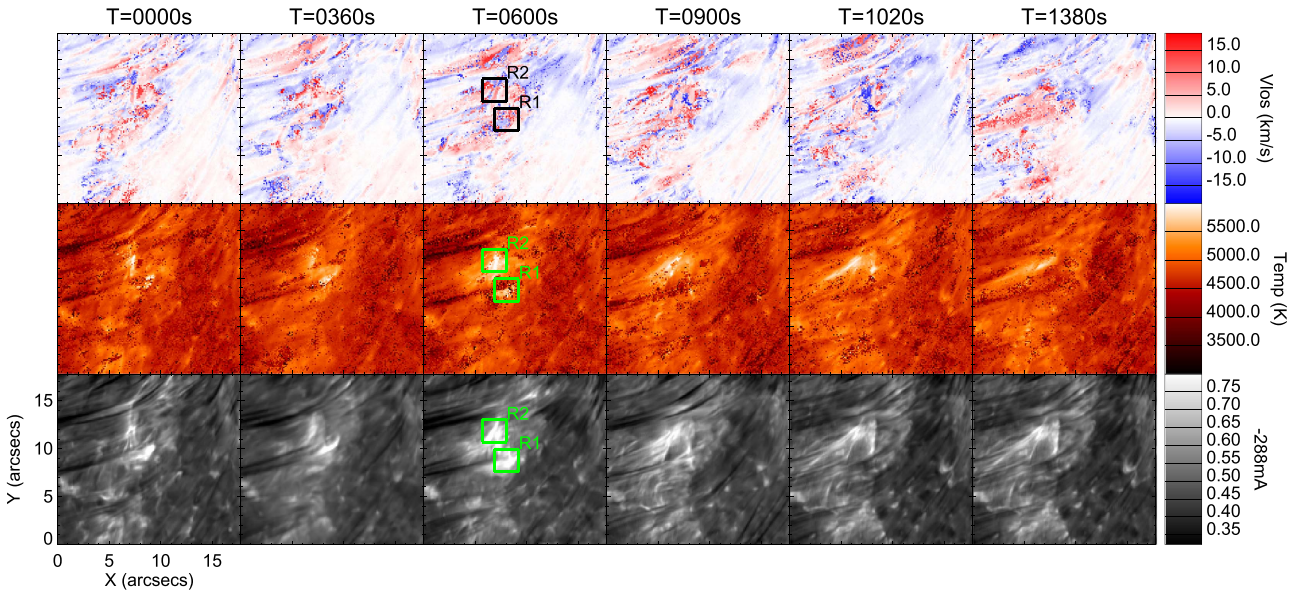

Figure 4. Top: the line-of-sight velocity outputs averaged between $\log(\tau) = -3$ and $\log(\tau) = -4$. Middle: the temperature output averaged over the same optical depth range. Bottom: the observed Stokes-*I* −288 mÅ images. The FOV is identical to the red box of Figure 1.

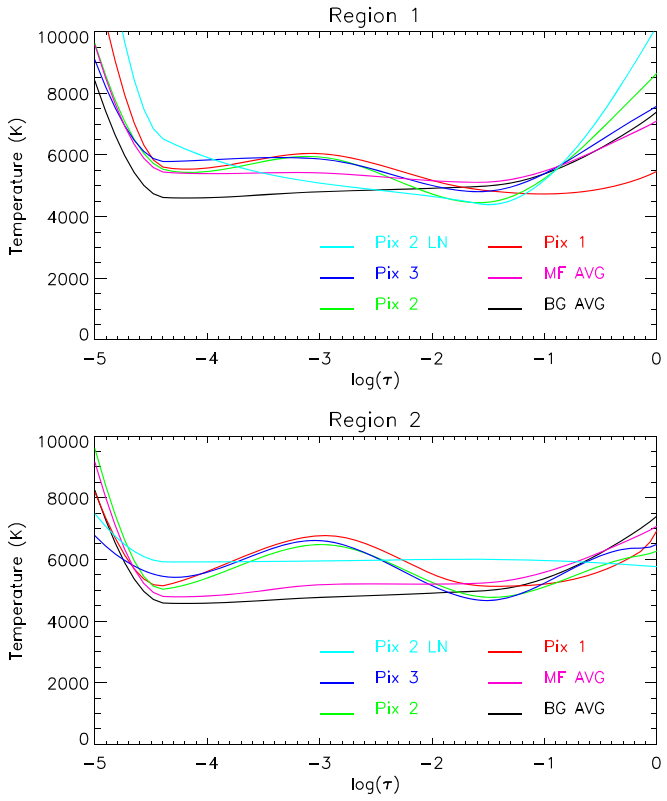

Figure 5. Temperature profiles of various pixels within R1 and R2, compared to the region average (MF AVG) and background average (BG AVG). Pix 2 LN shows the 4 node output for Pix 2.

area within the red box of Figure 1 was used for the inversions and was spatially binned 2×2. The profiles were normalized to a reference profile, taken from areas of quiet-Sun over the whole FOV, and averaged over the whole timeseries. The profiles were then interpolated onto a wavelength grid with 36 mÅ spacing between points. The weights for Stokes-Q and -U were made to be half that of Stokes-I and -V. Non-observed points in the interpolated profiles are given a negligible weight.

In order to improve convergence while maintaining many degrees of freedom, a staggered approach is taken, which is similar to that discussed in Ruiz Cobo & del Toro Iniesta (1992). The staggered approach uses an initial inversion, considering a lower number of nodes to get to a reasonable answer, albeit with little vertical stratification. The output model from this can then be used as the input guess model in a second inversion with more nodes.

The initial inversions, named "4 node" inversions, consisted of four nodes in temperature, three nodes in line-of-sight velocity, one node in line-of-sight magnetic field, and one node in microturbulence. An example output frame of this can be seen in Figure 2. The fitted Stokes-I line profile is quite good, with the temperature profile accurately mapping the brightened chromospheric structure. The Stokes line profiles shown in panels 3 and 4 of Figure 2 are taken from a pixel at the base of the connected fibril brightening with the micro-flaring structure. By only allowing one value of magnetic flux density over the formation height of the whole line, the synthetic profiles cannot map depth dependent magnetic flux regions. There appears to be a temperature enhancement throughout the brightened area. The line-of-sight velocity appears to show bi-directional flows at the micro-flare location, up to $20\,\mathrm{km\,s^{-1}}$,

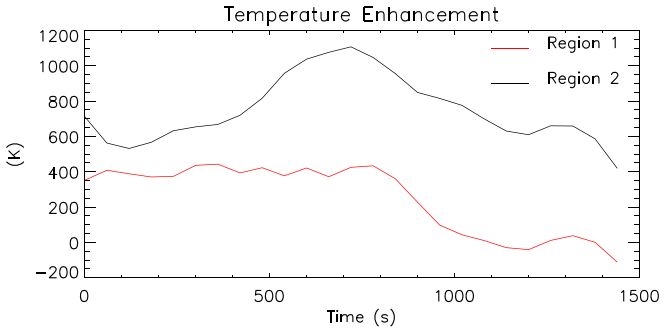

Figure 6. Mean temperature enhancements of the micro-flaring regions over time. This was measured over a slab between $\log(\tau) = -3$ and $\log(\tau) = -4$.

which are mainly in the chromosphere. The microturbulence appears to be quite large (up to $\sim 20\,\mathrm{km\,s^{-1}}$) in some unsuccessfully inverted regions, and around $10\,\mathrm{km\,s^{-1}}$ in the brightened region. This implies that with more nodes, a better fitting could be achieved in the temperature, velocity, and magnetic flux density, thus reducing the amount of unresolved microturbulence.

This output model was then smoothed before being fed into a new inversion with more nodes. This process spatially smooths the changes in the atmosphere introduced by the code by measuring the difference between the output model and the initial guess model from the 4 node inversion. This smoothed difference is then reapplied to the initial guess model (following J. de la Cruz Rodríguez 2017, private communication). The new inversion uses seven nodes in temperature (named "7 node") in an attempt to identify local fine thermal stratification in the atmosphere. Five nodes in line-of-sight velocity are also used, with three nodes in line-of-sight magnetic field, that allow for different flux densities in the photosphere than the chromosphere. One node is also used in the transverse magnetic field, though the weights are lessened here due to the noisiness of the Stokes-Q and -U profiles. Again, one node is applied in microturbulence. In this inversion, the regularization is reduced slightly to allow for increased vertical stratification.

The output for the 7 node inversion can be seen in Figure 3. The fitting of the line profiles is better than from the 4 node. There appears to be very little transverse magnetic fields present in the micro-flaring region, which is similar to that reported for EBs in Reid et al. (2016). The line-of-sight magnetic field appears to weaken in the higher atmospheric heights, as would be expected with magnetic flux densities between the photosphere and the chromosphere. The thermal enhancement still appears to exist, with higher contrast in the brightened region in the chromosphere. The line-of-sight velocity fields still show the bi-directional Doppler shifts and look very similar to the 4 node output. However, the downflow related to the connected brightened fibril structure is now apparent. The microturbulence appears to be much weaker in the 7 node inversion, reaching no more than $3.5\,\mathrm{km\,s^{-1}}$, and completely removing the very high, saturated regions ($20\,\mathrm{km\,s^{-1}}$) present in the 4 node inversions. This is due to the increased temperature nodes, allowing for a better fitting of the thermal broadening.

4. Inversion Results

The inversions were run in steps of 2 scans (~60 s). Initially, it was thought that by setting the initial guess model for an

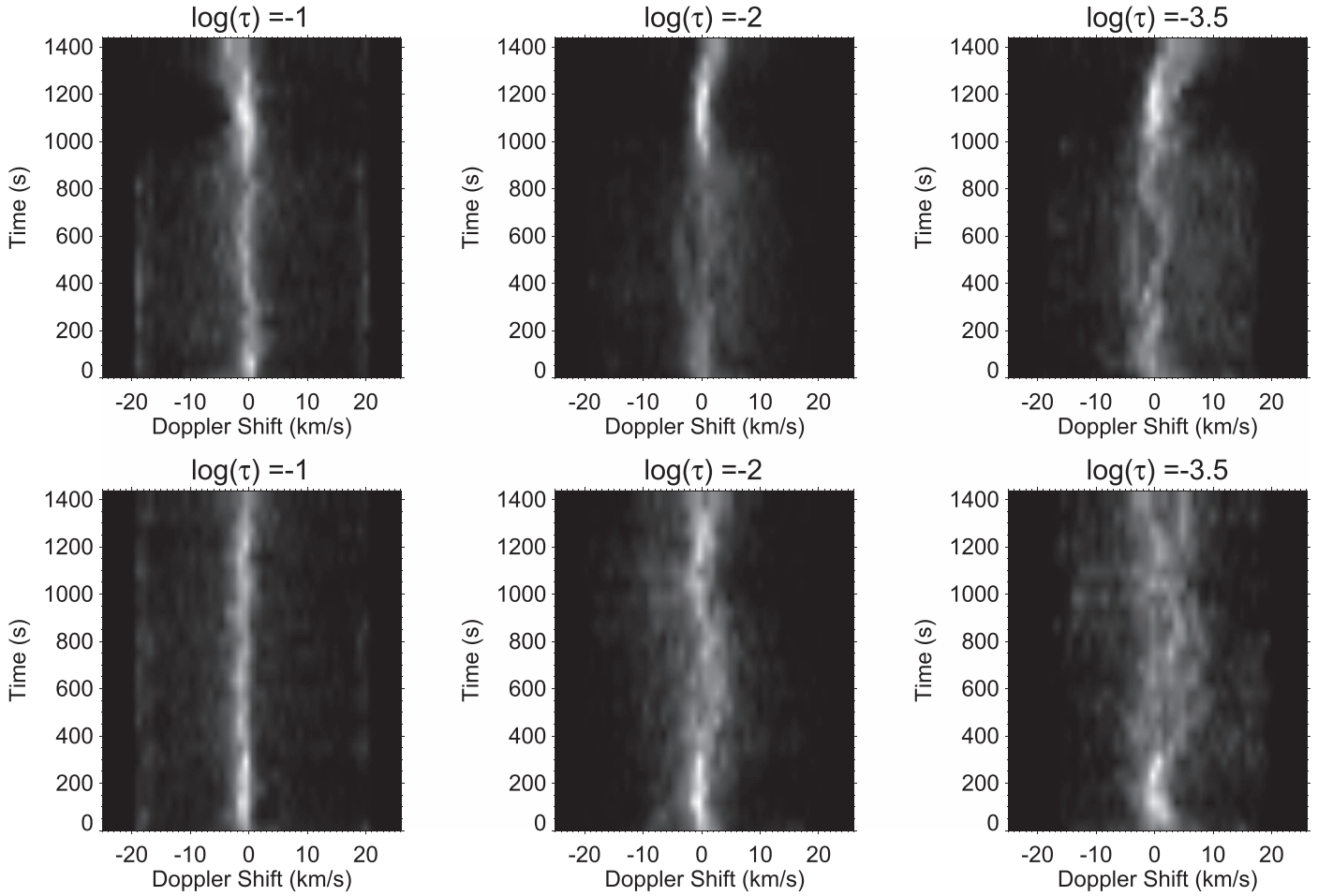

Figure 7. Velocity maps showing the Doppler shifts over time. Brightness indicates pixel density within the bin. The top row shows R1, while the bottom row shows R2.

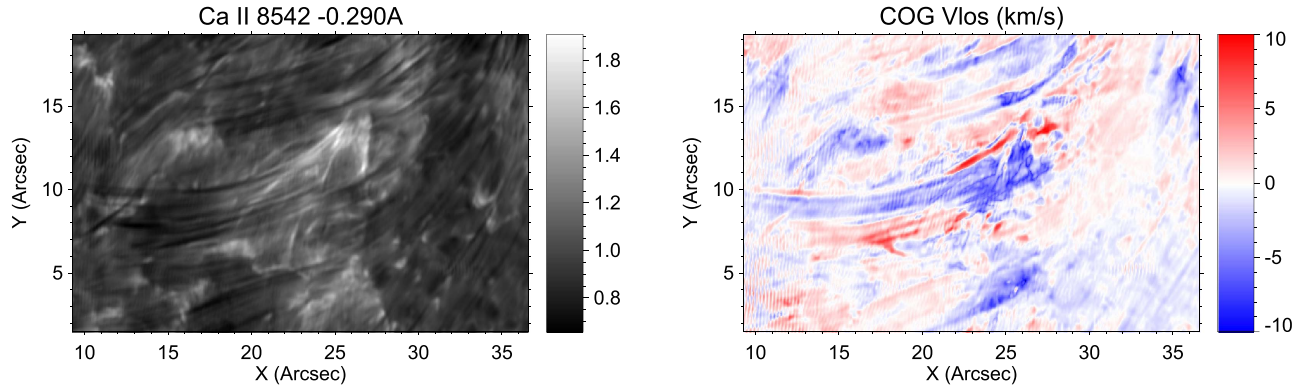

Figure 8. Left: the observed micro-flaring region with the associated fibril. Right: the line-of-sight velocity obtained via the center of gravity method. The frame chosen is identical to that of Figures 2 and 3.

inversion to be the smoothed output model from the previous frame, a better convergence could be achieved. However, it appeared to only restrict the possible outcomes in the dynamic event. With 60 s between frames, the scene can vary largely, and the best contrast and fitting of the line profile was found when the 4 node inversions for all frames used the same initially inverted output that used the FALC model (Fontenla et al. 1993) as the initial guess. This initial inversion was done for the median time frame during the lifetime of the event. The microturbulence was reset and the output of this inversion was also smoothed spatially to avoid excess inversion noise.

The outputs of the inversions can be seen in Figure 3 for $T = 1020$ s, while Figure 4 shows the inversion outputs over time. The animation of Figure 2 also presents detailed inversion outputs. R1 appears to be heated first, with a morphology similar to that of EBs (Watanabe et al. 2011), while R2 appears to get heated later in the timeseries. Both regions appear to be connected to a dark chromospheric fibril structure. Figure 4

Table 1
Magnetic Flux Cancellation Measurements Made for the Brightened Regions (R1 and R2), for the 4 Node and 7 Node Outputs

	R1 (4 node)	R2 (4 node)	R1 (7 node)	R2 (7 node)
Overall	$(8.89 \pm 1.90) \times 10^{16}$	$(-4.02 \pm 0.92) \times 10^{16}$	$(1.57 \pm 0.32) \times 10^{17}$	$(-9.73 \pm 2.04) \times 10^{16}$
Positive	$(1.97 \pm 0.42) \times 10^{11}$	$(-5.76 \pm 1.38) \times 10^{11}$ Mx s^{-1}	$(5.19 \pm 1.30) \times 10^{15}$	$(2.39 \pm 0.55) \times 10^{15}$
Negative	$(8.80 \pm 1.75) \times 10^{16}$	$(-3.98 \pm 0.76) \times 10^{16}$	$(1.42 \pm 0.31) \times 10^{17}$	$(-9.97 \pm 2.39) \times 10^{16}$

Note. The overall flux cancellation is shown, alongside the positive and negative polarity flux cancellation values. Values shown are in Mx s^{-1}.

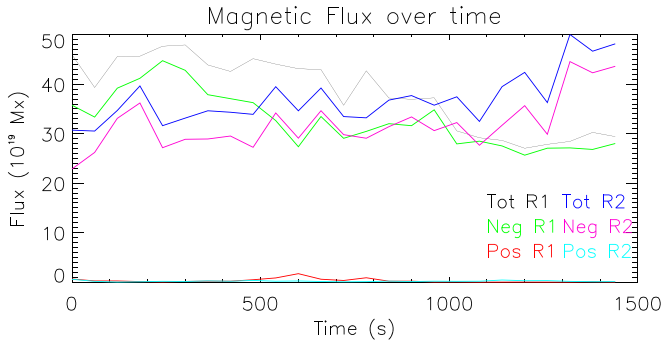

Figure 9. Magnetic flux over time. "Tot" = total flux, "Pos" = positive flux only, and "Neg" = negative flux only. R1 and R2 refer to the areas shown in the bottom right panel of Figure 1.

shows that as R2 evolves and becomes stronger, the length of heating along the fibril also increases. The propagation of the heating along the fibril appears to occur at a rate of ~6 km s^{-1}.

First, the temperature profile was investigated. A 20 binned pixel^2 box was placed around the brightened footpoints (R1 and R2). The average temperature profile could be taken for successfully inverted pixels to attain how the average temperature in the micro-flaring regions change over time. Figure 5 shows the average temperature profile compared to the background profile. The BG AVG profile (the black line) is taken as the background average of those pixels not affected by the flaring event, while the MF AVG profile (the pink line) is the average taken from the micro-flaring region. Three individual pixels from across the brightenings are also shown to present the temperature profiles for successfully inverted pixels. One of the pixels from the 4 node inversion is also shown (LN).

The average profile shows temperature rises in the chromosphere and photosphere, with a slight gradient. When looking at individual pixels, it appears as though NICOLE found its best fits when inserting chromospheric temperature bumps around $\log(\tau) = -3.5$. The temperature outputs were then averaged between $\log(\tau) = -3$ and $\log(\tau) = -4$, and the temperature enhancements relative to the background average calculated. Figure 6 shows the relative temperature enhancements for both micro-flaring regions. R2 shows more consistent, stronger temperature enhancements throughout the event, while at $T = 850$ s, R1 reaches the end of its lifetime. The mean temperature enhancements for R1 and R2 are 400 and 750 K during their lifetimes, respectively, though the central pixels chosen in Figure 5 show that the temperature enhancements are concentrated in the brightening and can reach 2000 K.

Figures 2 and 3 appear to show strong bi-directional Doppler shifting in the local area during the event. To check the Doppler shifting in the event over time, 1 km s^{-1} bins were created up to ±25 km s^{-1}. A box was then placed around R1 and R2, and each pixel placed into a bin. This was done over all inverted frames, at three different optical depths, again averaged over 1 dex. Figure 7 shows the output from this in both regions from the 7 node outputs. R1 shows strong chromospheric redshifting throughout the event, which is concentrated toward the end of the observations. R2 however appears to show a near equal amount of red- and blueshift in the chromosphere. Figure 3 shows that while strong blueshifting appears around the heated region (R2), the heated area, which follows the connected fibril, appears redshifted. The low sensitivity to the photosphere that is sampled in the line wings is apparent at $\log(\tau) = -1$. The extrapolation of the velocity estimates from the chromosphere pushes some of the pixels to extreme ±20 km s^{-1} values.

Center of gravity (COG) measurements (Uitenbroek 2003) were also used to determine the Doppler shifting of the observed line profiles at the heated fibril location. The results match the inversion outputs, showing a redshift of the heated region of the fibril (~up to 15 km s^{-1}). Figure 8 shows the observations of the fibril region along with the relative line-of-sight velocity measurements from the COG method.

This strong downflow measurement appears to continue throughout the brightened region of the fibril, while the rest of the fibril is only slightly redshifted. The brightened regions of R2 are constantly redshifted rather strongly, while this effect is more subtle with R1.

The magnetic flux was also investigated for the two regions. Using the same box as for the velocity and temperature measurements, the flux evolution is plotted for the two regions and for the different polarities in Figure 9. These values are from the 7 node inversions and averaged over 1 dex, centered around $\log(\tau) = -3.5$. The flux cancellation values can be seen in Table 1.

The overall flux for the 4 node output in R1 is lessened, with the majority of this flux cancellation occurring in the negative polarity, with the positive-polarity fields appearing negligible. The 4 node output for R2 tells a different story. Rather than showing evidence of flux cancellation, the opposite is apparent. Again, this is predominately due to the negative magnetic flux, with the positive-polarity flux difference being 5 orders of magnitude less.

In the 7 node inversions, the magnetic output from the inversions contained some depth with 3 nodes in line-of-sight magnetic flux density. At $\log(\tau) = -3.5$, R1 appears still appears to have strong magnetic flux cancellation. This is again mainly due to the negative polarity flux difference, with the positive-polarity flux cancellation appearing stronger than that of the 4 node outputs. The overall flux cancellation rate is strongest around $\log(\tau) = -3.5$, with weaker values in the photosphere below. R2 again shows flux growth due to strong enhancement in the negative polarity flux. The positive-polarity flux did show some weak flux cancellation in the 7 node outputs at this optical depth. Again, these values are weakened at higher optical depths.

5. Discussion and Conclusions

We have shown evidence of a localized chromospheric brightening with footpoints extending down to the upper photosphere, connecting to a chromospheric fibril. Using NICOLE inversions, we were able to show localized temperature enhancements in the low-mid-chromosphere of the order of ~1000 K, with no upper atmospheric response apparent. However, an overlying filament structure, which is present in the *SDO* AIA data, could mask any signal of this event at higher atmospheric heights. The temperature values are very mild in comparison to the previous literature on micro-flares. The localized temperature enhancement bumps are very similar to that shown in previous modeling efforts of EBs (e.g., Berlicki & Heinzel 2014; Reid et al. 2017), in shape and magnitude, and only occurring slightly higher in the atmosphere, thus disturbing the Ca II 8542 Å line core formation in the mid-chromosphere. The heated region also appeared to have the electron density increase tenfold (up to 10^{13} cm^{-3} in the low-mid-chromosphere). The localized temperature enhancements and velocity values are most similar to that of EBs in Figure 7 of Hansteen et al. (2017), and do not reach the strong temperatures and velocities of their UV bursts and small-flare examples that stretch into the transition region and corona.

Two regions were identified as the footpoints of this event, both showing temperature increases and connections to the overlying fibril. Weaker temperature enhancements were more apparent in one of the footpoints (R1) than its counterpart (R2). Figure 4 appears to show a strong overlying chromospheric canopy at the location of R1 (most apparent in $T = 600$ s). This reduction in intensity in the core and near wings of the Ca II 8542 Å line reduces the strength of the temperature response function for the chromosphere, resulting in weaker temperature enhancements. Instead, the cooler overlying structure is identified and masks the event. The temperature enhancements presented from the inversions should then be treated as a lower boundary.

Flux cancellation was apparent from the outputs of the inversions for one of the two heated footpoints studied (R1). This is stronger than that of typical EBs (Reid et al. 2016) or moving magnetic features (MMFs; Nelson et al. 2016). R2, however, appeared not to show any evidence for flux cancellation, perhaps due to the more complex nature of the event and its stronger connection to the overlying fibril. No strong change in magnetic flux was observed via the line-of-sight magnetograms from HMI. This may be due to the low formation height of the 6173 Å line sampled by HMI or the relatively low resolution of the instrument in comparison to ground-based instrumentation.

Initially, R2 had a relatively weak Ca II 8542 Å line enhancement in comparison to its eruptive counterpart (R1). However, as the brightening of R2 changed morphology and it connected to the chromospheric fibril, very strong, impulsive heating occurred at the base of this connection (up to ~2000 K). The heating progressed along the fibril at a rate of ~6 km s^{-1}. This is similar to the extension speed of the EB "flame" morphology in the photosphere (Watanabe et al. 2011).

The heated regions connecting to the fibril also show apparent downward, redshifted motion of the order of 10–15 km s^{-1}. Figure 3 hints that there may be up-flowing material below $\log(\tau) = -3.5$. This may interact with the chromospheric canopy to form this brightening. If this was an upwardly moving positive-polarity magnetic flux region, this could be evidence of a form of chromospheric reconnection similar to previous micro-flares and to mechanisms describing EB formation (Georgoulis et al. 2002). This would also explain the chromospheric flux reduction for the negative polarity, but not for the positive polarity, as the positive-polarity flux region moved into this portion of the atmosphere. However, due to the weaker contribution of the Ca II 8542 Å line to the photosphere compared to the chromosphere, combined with the low signal from circular polarization, obtaining accurate photospheric magnetic fields would require co-temporal spectropolarimetry from another spectral line. In this particular case, there seems to be a pre-existing, overhanging canopy (e.g., see the beginning of the animation of Figure 1 for the best impression), of which part then connects to the lower EB flame. The downflow in the upper fibril (connecting to R2) could indicate a draining of the pre-existing canopy post reconnection.

While strict nomenclature exists to differentiate between a plethora of solar events, we postulate that the difference between this event (named as a micro-flare due to its chromospheric signatures) is identical to that of an EB, with the only difference being that this event is slightly higher in the atmosphere than a traditional EB, causing the moustache line profile normally associated with EBs to be skewed. Due to this event occurring slightly higher in the atmosphere than typical EBs, the usual EB "flame" morphology interacts with the chromospheric canopy, suggesting that not all EB reconnection events are purely photospheric in nature.

We thank the anonymous referee the valuable comments that improved the manuscript. We would also like to thank Jaime de la Cruz Rodríguez for valuable input into the NICOLE inversion code. Armagh Observatory and Planetarium is grant-aided by the N. Ireland Department for Communities. The Swedish 1 m Solar Telescope is operated on the island of La Palma by the Institute for Solar Physics of Stockholm University in the Spanish Observatorio del Roque de los Muchachos of the Instituto de Astrofísica de Canarias. The authors wish to acknowledge the DJEI/DES/SFI/HEA Irish Centre for High-End Computing (ICHEC) for the provision of computing facilities and support. A.R. would like to thank Armagh Observatory and Queen's University Belfast for funding. The research leading to these results has received funding from the European Community's Seventh Framework Programme (FP7/2007–2013) under grant agreement No. 606862 (F-CHROMA). Research at the Armagh Observatory is grant-aided by the Northern Ireland Department of Communities.

References

Archontis, V., & Hansteen, V. 2014, ApJL, 788, L2
Archontis, V., & Hood, A. W. 2009, A&A, 508, 1469
Berkebile-Stoiser, S., Gömöry, P., Veronig, A. M., Rybák, J., & Sütterlin, P. 2009, A&A, 505, 811
Berlicki, A., & Heinzel, P. 2014, A&A, 567, A110
Berlicki, A., Heinzel, P., & Avrett, E. H. 2010, MmSAI, 81, 646
Brosius, J. W., & Holman, G. D. 2010, ApJ, 720, 1472
Cauzzi, G., Falchi, A., & Falciani, R. 2001, SoPh, 199, 47
Cauzzi, G., Reardon, K. P., Uitenbroek, H., et al. 2008, A&A, 480, 515
Chen, F., & Ding, M. D. 2010, ApJ, 724, 640
Chifor, C., Isobe, H., Mason, H. E., et al. 2008, A&A, 491, 279
de la Cruz Rodríguez, J., Löfdahl, M., Sütterlin, P., Hillberg, T., & Rouppe van der Voort, L. 2015, A&A, 573, A40
Ellerman, F. 1917, ApJ, 46, 298

Fang, C., Tang, Y. H., Xu, Z., Ding, M. D., & Chen, P. F. 2006, ApJ, 643, 1325
Fontenla, J. M., Avrett, E. H., & Loeser, R. 1993, ApJ, 406, 319
Georgoulis, M. K., Rust, D. M., Bernasconi, P. N., & Schmieder, B. 2002, ApJ, 575, 506
Gontikakis, C., Winebarger, A. R., & Patsourakos, S. 2013, A&A, 550, A16
Grubecka, M., Schmieder, B., Berlicki, A., et al. 2016, A&A, 593, A32
Hannah, I. G., Hudson, H. S., Battaglia, M., et al. 2011, SSRv, 159, 263
Hansteen, V. H., Archontis, V., Pereira, T. M. D., et al. 2017, ApJ, 839, 22
Henriques, V. M. J. 2012, A&A, 548, A114
Hong, J., Ding, M., Li, Y., Fang, C., & Cao, W. 2014, ApJ, 792, 13
Hong, J., Ding, M. D., Li, Y., et al. 2016, ApJL, 820, L17
Isobe, H., Tripathi, D., & Archontis, V. 2007, ApJL, 657, L53
Jess, D. B., Mathioudakis, M., Browning, P. K., Crockett, P. J., & Keenan, F. P. 2010, ApJL, 712, L111
Jiang, R. L., Fang, C., & Chen, P. F. 2010, ApJ, 710, 1387
Jiang, R.-L., Fang, C., & Chen, P.-F. 2012, in EAS Publications Ser. 55, Magnetic Reconnection in a Canopy-type Magnetic Configuration for Solar Microflares, ed. Faurobert et al. (Les Ulis: EDP Sciences), 107
Kano, R., Shimizu, T., & Tarbell, T. D. 2010, ApJ, 720, 1136
Leenaarts, J., de la Cruz Rodrguez, J., Kochukhov, O., & Carlsson, M. 2014, ApJL, 784, L17
Leiko, U. M., & Kondrashova, N. N. 2015, AdSpR, 55, 886
Lemen, J. R., Title, A. M., Akin, D. J., et al. 2012, SoPh, 275, 17
Li, Z., Fang, C., Guo, Y., Xu, Z., & Cao, W. 2015, RAA, 15, 9
Löfdahl, M. G. 2002, Proc. SPIE, 4792, 146L
Matsumoto, T., Kitai, R., Shibata, K., et al. 2008, PASJ, 60, 577
Nelson, C. J., Doyle, J. G., & Erdélyi, R. 2016, MNRAS, 463, 2190
Reid, A. L., Mathioudakis, M., Doyle, J. G., et al. 2016, ApJ, 823, 110
Reid, A. L., Mathioudakis, M., Doyle, J. G., et al. 2017, ApJL, 835, L37
Reid, A. L., Mathioudakis, M., Scullion, E., et al. 2015, ApJ, 805, 64
Ruiz Cobo, B., & del Toro Iniesta, J. C. 1992, ApJ, 398, 375
Rutten, R. J. 2003, Radiative Transfer in Stellar Atmospheres, Lecture Notes (Utrect Univ.)
Rutten, R. J., Vissers, G. J. M., Rouppe van der Voort, L. H. M., Sutterlin, P., & Vitas, N. 2013, J. Physics Conf. Series, 440, 012007
Scharmer, G. B., Bjelksjo, K., Korhonen, T. K., Lindberg, B., & Petterson, B. 2003, Proc. SPIE, 4853, 341
Scharmer, G. B., Narayan, G., Hillberg, T., et al. 2008, ApJL, 689, L69
Schnerr, R. S., de La Cruz Rodríguez, J., & van Noort, M. 2011, A&A, 534, A45
Schou, J., Scherrer, P. H., Bush, R. I., et al. 2012, SoPh, 275, 229
Shimizu, T. 2011, in IAU Symp. 273, Physics of Sun and Star Spots, ed. D. Prasad Choudhary & K. G. Strassmeier (Cambridge: Cambridge Univ. Press), 157
Shine, R. A., Title, A. M., Tarbell, T. D., et al. 1994, ApJ, 430, 413
Socas-Navarro, H., de la Cruz Rodriguez, J., Asensio Ramos, A., Trujillo Bueno, J., & Ruiz Cobo, B. 2015, A&A, 577, A7
Socas-Navarro, H., Ruiz Cobo, B., & Trujillo Bueno, J. 1998, ApJ, 507, 470
Socas-Navarro, H., & Trujillo Bueno, J. 1997, ApJ, 490, 383
Uitenbroek, H. 2003, ApJ, 592, 1225
van Noort, M., Rouppe van der Voort, L., & Löfdahl, M. G. 2005, SoPh, 228, 191
Vissers, G. J. M., van der Voort, L. H. M., & Rutten, R. J. 2013, ApJ, 774, 32
Watanabe, H., Kitai, R., Okamoto, K., et al. 2008, ApJ, 684, 736
Watanabe, H., Vissers, G., Kitai, R., van der Voort, L. R., & Rutten, R. J. 2011, ApJ, 736, 71
Yang, H., Chae, J., Lim, E.-K., et al. 2013, SoPh, 288, 39
Zuccarello, F., Guglielmino, S. L., & Romano, P. 2011, MmSAI, 82, 149